Available online at www.sciencedirect.com

ScienceDirect

Proceedings of the Combustion Institute 38 (2021) 3899–3907

Proceedings of the Combustion Institute

www.elsevier.com/locate/proci

Simultaneous in-situ measurements of gas temperature and pyrolysis of biomass smoldering via X-ray computed tomography

Emeric Boigné [a,*], N. Robert Bennett [b], Adam Wang [b], Khadijeh Mohri [c], Matthias Ihme [a]

[a] *Department of Mechanical Engineering, Stanford University, Stanford, CA 94305, United States*
[b] *Department of Radiology, Stanford University, Stanford, CA 94305, United States*
[c] *Institute for Combustion and Gas Dynamics, University of Duisburg-Essen, Duisburg 47057, Germany*

Received 7 November 2019; accepted 28 June 2020
Available online 17 September 2020

Abstract

In-situ X-ray computed tomography (XCT) imaging is employed to investigate the smoldering dynamics of biomass at the sub-millimeter scale. This technique provides simultaneous and spatially-resolved information about the gas temperature and the biomass density, thereby enabling tracking of the pyrolysis and char oxidation fronts. To achieve well-controlled heating and flow conditioning, oak biomass samples are instrumented above a diffusion flame inside a tube, with total oxygen concentrations of 6% and 11% per volume. Experiments are performed on a laboratory XCT system. The flow is diluted with Kr to increase X-ray attenuation in the gas phase thus allowing for simultaneous 3D measurements of sample density and surrounding temperature. XCT scans are acquired every 90 s at a spatial resolution of 135 μm. The high spatial resolution enables the volumetric visualization of the smoldering process that is associated with pyrolysis and char oxidation. These measurements show how the grain structure affects flame stabilization and induces fingering of the pyrolysis front, while crack formation accelerates the char oxidation locally. Evaluations of the sample mass via XCT are compared with load cell measurements, showing good agreement. A low-order model is developed to evaluate the propagation speeds of pyrolysis and oxidation fronts from the X-ray data over time, and comparisons are made with the surface recess speed.

Keywords: Smoldering; Heterogeneous combustion; Pyrolysis; Biomass; X-ray computed tomography

1. Introduction

Smoldering is estimated to contribute to more than 50% of the biomass consumed in wildfires [1]. Smoldering plays a key role in peat fires, representing an equivalent of about 15% of the total

* Corresponding author.
E-mail address: eboigne@stanford.edu (E. Boigné).

https://doi.org/10.1016/j.proci.2020.06.070

anthropogenic greenhouse-gas emissions [2]. In the context of wood fires, the transport of ember can accelerate fire spread, while larger logs can smolder for many days after flaming, and potentially restart fires [3]. Apart from its direct relevance to fire safety and wildland fires, combustion of biomass is also relevant for energy production, as it represents a low-carbon feedstock [4].

Smoldering depends strongly on the heat exchange with the surrounding environment, ambient oxygen concentration, permeability, and density, as well as the content of moisture and inorganic material in the fuel [1,5]. Kinetic models for biomass smoldering have been developed [6], in which the exothermic smoldering is described by reaction mechanisms consisting of (I) an endothermic pyrolysis step, that is followed by (II) the heterogeneous and exothermic char oxidation [1]:

$$\text{Biomass(s)} \xrightarrow{+\text{Heat}} \text{Char(s)} + \text{Pyrolyzate(g)}, \quad \text{(I)}$$

$$\text{Char(s)} + \text{O}_2\text{(g)} \underset{-\text{Heat}}{\longrightarrow} \text{Ash(s)} + \text{Products(g)}. \quad \text{(II)}$$

While the primary reaction pathways are well understood, establishing reliable data for pyrolysis and oxidation rates as well as the description of flaming and extinction events remain a focus of active research [1,7,8]. Experiments have been conducted to obtain global information, typically by measuring mass loss rates, or using 1D arrays of thermocouples [7]. The multiphase nature of smoldering processes introduces limitations on optical access, and achieving volumetrically resolved measurements remains a challenge. Optical cameras have been used to monitor exterior surface fronts and image smoldering instabilities in narrow channels [9]. In addition, infrared techniques have been employed to capture the oxidation front during the smoldering of peat [10]. By using 2D arrays of microphones and speakers, ultrasound measurements were conducted to examine the averaged permeability of polyurethane foams during smoldering [11,12]. Although this technique provides valuable information about the dynamics of smoldering, it is limited by its spatial resolution (10 mm), low dynamic range, and the restriction to highly permeable media.

One-dimensional simulations have been performed to model the kinetics of smoldering [6,7], and 2D simulations of experiments have been performed. The transition to flaming was successfully captured for cellulosic insulation via simulations [13]. By simulating the smoldering of polyurethane foams, Scott et al. [14] demonstrated the importance of accurately representing the multi-dimensional heat exchange, mass and momentum transfers, in addition to the chemical kinetics.

X-ray computed tomography (XCT) is a technique that allows for the penetration of dense materials in order to image their 3D structures. Common XCT systems include (i) laboratory systems with sub-millimeter resolution and fast acquisition times [15], (ii) micro-CT systems providing micrometer resolution but slow acquisition times (at least several hours) [16], and (iii) synchrotron sources allowing for both sub-micrometer resolution and fast acquisition times, at the expense of a limited field of view [17]. In the past, the structure of coal has been examined by XCT [16,18]. Synchrotron XCT was applied to image biochar after pyrolysis, showing the effect of the pyrolysis temperature on the char structure [19]. However, these 3D XCT studies have only focused on characterizing the solid structures pre- and post-combustion. So far, in-situ measurements of smoldering via X-ray imaging only considered radiography measurements of polyurethane foam [20].

Recent advances in X-ray systems offer opportunities for probing the dynamics of multiphase processes at high spatial and temporal resolutions [21]. Combined with recent developments of quantitative gas phase temperature measurements in the form of X-ray absorption [15,22], and X-ray fluorescence [17], XCT provides opportunities for simultaneous and time-resolved in-situ measurements of biomass smoldering. Therefore, the objective of the present work is to develop and employ XCT for in-situ 3D imaging of smoldering. For this, XCT absorption measurements are acquired using a X-ray laboratory system. The experimental method is presented in Section 2, and the setup is described in Section 3. Quantitative measurements of gas phase temperature and solid density during the smoldering process are performed and results are presented in Section 4. Conclusions are presented in Section 5.

2. Experimental method

2.1. X-ray computed tomography

In this work, X-ray absorption tomography is employed. In this technique, the absorbed beam intensity is related to the incident intensity via the Beer–Lambert law [23]. In XCT, measurements are acquired over numerous angles, enabling a 3D reconstruction of the linear attenuation field. At a location $\boldsymbol{x}$ and time t, the linear attenuation μ is related to the local density ρ via $\mu(\boldsymbol{x}, t) = \zeta(\boldsymbol{x}, t)\rho(\boldsymbol{x}, t)$, where ζ is the mass attenuation coefficient which depends upon the local atomic composition and can be evaluated from tables [23].

2.2. Solid density measurements

Differences in the linear attenuation μ between oak biomass, char, and gases can be employed to distinguish between different combustion states, and separate the reaction fronts associated with pyrolysis and oxidation. This is illustrated in Fig. 1,

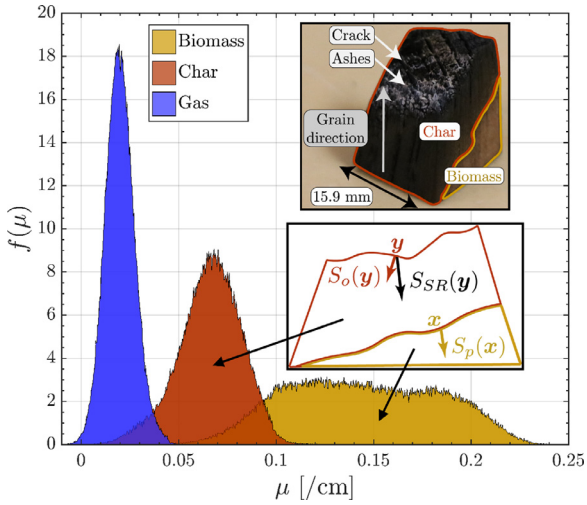

Fig. 1. Histogram of X-ray attenuation μ for 18,000 voxels in gas phase, char and oak biomass regions showing contrast for the selective detection of material density. The figure also includes (top) an illustration of a burnt sample highlighting the grain direction, and (bottom) a schematic of the propagation of pyrolysis and oxidation within a cross-section of the sample, with pyrolysis speed S_p, char oxidation speed S_o, and speed of surface recess S_{SR}.

showing a histogram of attenuation μ for three distinct regions. The X-ray attenuation in the gas phase can be related to the temperature, while the reduction in the attenuation from oak biomass to char is explained by the reduction in density. Oak biomass has a wider distribution due to density variations from grain structures. In the present work, gas and solid phases are segmented using a global threshold equal to 0.036 cm^{-1}, while local fluctuations in linear attenuation are tracked over time to localize the pyrolysis front separating oak biomass and char.

Calibration experiments are first performed to evaluate the mass attenuation coefficients ζ of the different materials in order to enable measurements of density ρ. For this, XCT measurements of known mass of oak biomass and char are acquired. Their volumes are evaluated using segmentation from the X-ray reconstructions, yielding mean densities $\rho_b = 617 \pm 30$ kg/m^3 for the oak biomass and $\rho_c = 204 \pm 10$ kg/m^3 for the oak char. By determining the linear attenuation from separate XCT measurements, the resulting mass attenuation coefficients are obtained as $\zeta_b = 0.242 \pm 0.015$ cm^2/g for the oak biomass and $\zeta_c = 0.254 \pm 0.016$ cm^2/g for the char. Given the small difference between the two materials, a mean value is used to infer the density from linear attenuation.

2.3. Gas phase temperature measurements

To obtain quantitative information about the gas phase temperature, simultaneous Kr-gas XCT measurements are performed. Because of their low atomic number, the X-ray absorption by ambient gas molecules such as N_2 and O_2 is negligible at the energy-levels accessible with the system used. In contrast, with a molecular weight of 83.8 g/mol, Kr attenuates X-rays approximately 100 times more than air at the energy levels considered. This signal is sufficient to be captured with the present system. The flow is therefore diluted with Kr, allowing the local gas phase temperature T_g to be determined from the linear attenuation as [15,22]:

$$T_g(\boldsymbol{x}) = T_{g,\mathrm{ref}} \frac{X_{\mathrm{Kr}}(\boldsymbol{x})}{X_{\mathrm{Kr,ref}}} \frac{\mu_{\mathrm{ref}}}{\mu(\boldsymbol{x})}, \tag{1}$$

where X_{Kr} is the mole fraction of Kr, and the subscript 'ref' denotes a reference state. Quantitative evaluations of temperature require a homogeneous Kr mole fraction $X_{\mathrm{Kr}}(\boldsymbol{x})$ in the flow. In the present work, the reactant streams were diluted with Kr at a mole fraction of $X_{\mathrm{Kr}} = 0.50$ to obtain sufficient signal intensity. Even with large concentrations of Kr, the gas attenuation remains small compared to attenuation in the solid phase, as seen from Fig. 1. This introduces uncertainties in the temperature measurements of $\pm 15\%$ at $T = 2000$ K and $\pm 5\%$ at ambient temperature [15]. Improvement in signal-to-noise ratios can be achieved by increasing exposure time, using lower X-ray energies as in mammography or dental XCT systems, or using synchrotron sources with higher photon counts. Alternatively, with X-ray fluorescence similar gas temperature uncertainties can be achieved at lower Kr concentrations [17,24].

In addition, Kr dilution introduces further errors in the temperature measured locally around

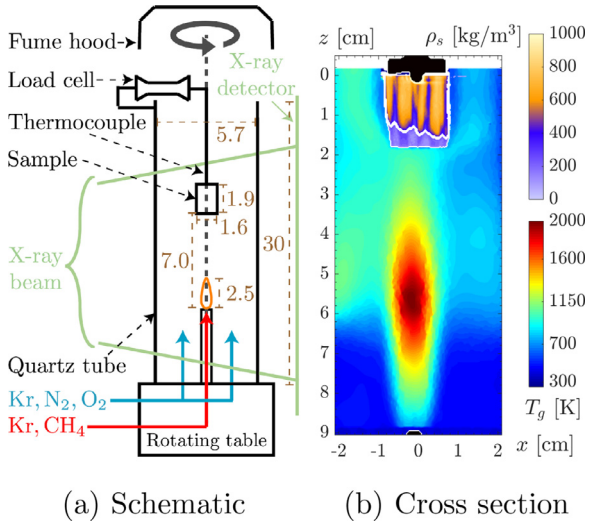

Fig. 2. (a) Schematic of the experimental setup with dimensions in centimeters, and (b) XCT cross section showing center-plane sample density ρ_s and gas temperature T_g during smoldering at time 6:10 [MM:SS] for 6% O_2. The pyrolysis front is shown by a white contour in (b).

the sample. Because of the release of volatile gases at the sample surface, the Kr mole fraction is locally reduced by dilution. Specifically, at the maximum consumption rate of 0.7 g/min observed in this work, and assuming a molar weight of volatile gases equal to that of CO_2, a relative 10% dilution can be estimated. This corresponds to a minimum Kr mole fraction of $X_{\mathrm{Kr}} = 0.45$, and a temperature overestimation of up to 10% near the sample. Although compromising high-fidelity gas temperature measurements, these errors remain of second order, and in the following a constant value of $X_{\mathrm{Kr}} = 0.50$ is used.

2.4. Pyrolysis, oxidation and surface recess speeds

From the in-situ XCT measurements, propagation speeds of pyrolysis S_p and char oxidation S_o are evaluated. They are defined with respect to the global mass flow rates of pyrolyzate gases $\dot{m}_p$ and oxidation gases $\dot{m}_o$ as

$$\dot{m}_p = (\rho_b - \rho_c) A_p S_p \,, \tag{2a}$$

$$\dot{m}_o = \rho_c A_o S_o \,, \tag{2b}$$

in which ρ_b and ρ_c are the densities of oak biomass and char, and A_p and A_o are the surface areas of the pyrolysis and char oxidation fronts. The surface recess speed S_{SR} of the sample is also determined from XCT measurements. A 3D image of these quantities is shown in Fig. 1. The pyrolysis and surface recess speeds measure the displacement of the pyrolysis and oxidation interfaces in the laboratory frame of reference. Surface recess speed is measured locally by computing the recess between XCT scans of the sample surface along the local surface normal direction. Due to shrinkage of the sample during pyrolysis, the char oxidation speed S_o cannot be directly evaluated from XCT measurements. A volumetric model to evaluate oxidation and pyrolysis speeds is thus developed. This model is discussed in Section 4.3.

3. Experimental setup

3.1. Experimental apparatus

Figure 2a provides a schematic illustration of the experimental apparatus, consisting of a sample confined in a quartz tube that is placed on a rotating table in a laboratory X-ray system. Figure 2b is a cross-section of XCT measurements and represents the oak biomass sample placed above the oxygen-diluted flame. The oak biomass sample is instrumented with a K-type thermocouple press-fit into it. The thermocouple, colored in black in Fig. 2b, is embedded 2 mm within the sample and provides an averaged solid temperature. A beam load cell is used to measure the mass of the sample during the experiment, with an uncertainty of 50 mg. The experiments are also continuously filmed with a DSLR camera. The presence of a visible flame in these images is used to distinguish between flaming and smoldering regimes.

To stabilize the smoldering and achieve well controlled conditions, a diffusion flame is used as a constant heat source. The sample is placed at a height $h = 7.0$ cm above the burner. An equimolar mixture of CH_4 and Kr is supplied through the

burner orifice of 2 mm diameter, at a mass flow rate of 0.48 g/min, corresponding to a firing rate of 71 W. The oxidizer is supplied by a coflow surrounding the burner with a mixture of Kr, O_2 and N_2, for a mass flow rate of 6.24 g/min. The area of the coflow is 25.4 cm^2. The Kr-mole fractions in both streams are identical at $X_{Kr} = 0.50$. The proportions of O_2 and N_2 are varied to control the oxidation rate while keeping the mass flow constant. The oxygen mole fraction at the sample height X_{O_2} is varied from 6% to 11%. The gases are supplied from gas cylinders and metered through mass flow controllers (Alicat Scientific). Uncertainties for all flow rates are evaluated to be less than 5%.

3.2. Oak biomass samples

The biomass samples consist of square cuboids of dried oak. Oak is a ring-porous hardwood, with distinct grain structures at the sub-millimeter scale. The heights of the samples are 19.0 ± 0.1 mm and the squared horizontal cross sections have a length of 16.0 ± 0.1 mm. A burnt sample is presented in Fig. 1, showing that the grain direction is aligned along the vertical flow direction. After machining, all samples are dried for five hours in an oven at 110 °C and kept in a desiccator to preserve their low moisture content. The average mass loss during drying is 6.1 ± 0.3%. A proximate analysis was performed after dying, which provides the following sample characterization: 83.4% volatile content, 11.5% fixed carbon, 4.23% moisture content, and 0.87% ashes.

We note that, without prior drying, the variation in X-ray attenuation is found to be sufficient to capture the primary propagation of a drying front before pyrolysis. However, this occurs at a rate of about 1 cm/min, which is too fast to be adequately resolved over time.

3.3. X-ray system and acquisition procedure

XCT measurements are performed on a table-top laboratory X-ray system, consisting of an X-ray tube, a collimator, a rotating table and a detector [15,22]. The X-ray tube is operated at 57 kV and 80 mA, chosen to reduce noise. The X-ray cone beam has a 12° half angle. The center of rotation of the object is placed at a distance of 48 cm away from the source focal spot, having a nominal size of 300 μm. The detector is placed at a distance of 69 cm from the source, for a geometric magnification of 1.44. The detector pixel size is 194 μm.

For each experiment, the flame is first stabilized inside the tube. At time 00:00 (MM:SS), the sample is placed in the tube, above the flame. Successive XCT scans are acquired approximately every 90 s. Each XCT scan lasts 30 s and consists of 225 images of 2048 × 1536 pixels acquired at 7.5 Hz, over a 360° rotation of the sample. The projection images are then used as input to a XCT reconstruction algorithm, to reconstruct the 3D field of solid density ρ_s and gas temperature T_g with an isotropic voxel size of 135 μm. Volume reconstructions are performed used the Feldkamp–Davis–Kress (FDK) algorithm, a standard direct method based on Fourier transforms for cone-beam XCT [25]. Further details on the XCT reconstruction procedure can be found in previous work [15].

A finite focal spot size and X-ray scattering lead to blurring by up to 7 voxels. To properly resolve the thermal boundary layer around the sample, normalization is performed by using calibration scans acquired without any Kr, reducing the blurring to 2–3 voxels. Additional blurring originates from the density changes in the sample due to on-going smoldering over the 30-s duration of each 360° rotation. Ideally, the X-ray acquisition should be performed simultaneously at all angles, for instance via multi-angle XCT systems [26]. However, such systems remain limited and only sequential acquisition is performed. A rotation rate of 12°/s is chosen to diminish the sample changes while providing sufficient photon counts. The propagation speeds of the reaction front measured in this work remains below 1.2 mm/min, corresponding to a maximum motion of 4.5 voxels over one rotation. Consequently the rotation speed is fast enough to reduce major changes of the sample over the duration of one CT acquisition, thereby preventing significantly larger artifacts.

4. Results and discussion

4.1. Sample mass and temperature

Sample temperature and mass are measured using a thermocouple and a load cell. Results are reported in Fig. 3 for 6% and 11% O_2. For both conditions, transition to flaming is observed within the first two minutes. For 6% O_2, the flaming is intermittent, and stable for only 3 min and 30 s. Stable smoldering is observed afterwards, with a monotonic increase in sample temperature. For 11% O_2, the flaming is significantly stronger and leads to complete pyrolysis within 5 min and 20 s. Once outgasing of flammable pyrolysis gases is completed, flaming ends and a smoldering regime follows, decaying in intensity as the solid temperature decreases. Both experiments are terminated at time 15:15 by manually stopping the fuel supply. After the experiments, the burnt sample consists of 45% char per volume for the 6% O_2 case, and pure char for the 11% O_2 case. The total mass of the sample is also evaluated by integrating the XCT density field over the sample. Comparisons of the mass inferred from the X-ray measurements, m_{XCT}, and load-cell measurements, m_{LC}, are also presented in Fig. 3, showing good agreement.

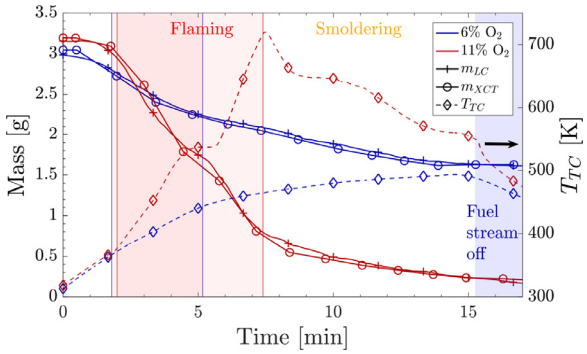

Fig. 3. Thermocouple temperature T_{TC} and total sample mass measured via load cell, m_{LC}, and inferred from XCT, m_{XCT}, over the duration of two experiments with different O_2 concentrations. Vertical lines delineate the flaming periods highlighted in red.

4.2. 3D solid density and gas temperature

The solid density and gas phase temperature of the smoldering oak samples are measured simultaneously via XCT. A representative cross-section acquired during smoldering is shown in Fig. 2b for 6% O_2 at time 6:10. The characteristic temperature field of a diffusion flame is well retrieved. The fresh gas region in the first two centimeters above the burner is not well captured because of XCT artifacts from the metallic burner. The samples are slightly offset from the center of the diffusion flame, leading to enhanced flaming on one side and a tilting of the propagation front, shown by the white contour in Fig. 2b. Repeatability of position is achieved to within 300 μm, evaluated from the XCT. The grain structure along the vertical direction within the sample is visible both upstream and downstream of the pyrolysis, with up to 50% density variations.

Figure 4 presents the surface recess speed S_{SR} of the sample, and zoomed views of cross-sections at different times for 6% and 11% O_2. The complex multidimensional surface recession during the smoldering is visible. First, in both cases, the pyrolysis begins at the bottom corners of the sample due to the locally larger surface exposed to the heat and oxygen environment. Second, small-scale structural variations within the biomass samples result in fingering of the pyrolysis front, which is clearly seen for 6% O_2 in Fig. 4 (white contour in the cross sections). Third, for 11% O_2, the formation of a crack within the brittle char is visible at 12:00. This crack enhances the oxidation by increasing the surface area and enabling transport of O_2 at 650 ± 50 K within the char. Fourth, transition to flaming occurs in both cases on the side for $x < 0$. Note that the temperature corresponds to the mean field over a 30-s acquisition window, averaged over the buoyant instabilities that are characteristic of flaming. For 6% O_2, flaming is intermittent between 1:40 and 5:10 and only a slightly higher gas temperature is seen in Fig. 4a (for the side $x < 0$ at 4:50). This is sufficient to result in a tilting of the pyrolysis front (7:30–14:30). For 11% O_2, strong flaming occurs between 2:00 and 7:20, first on the $x < 0$ side of the sample (4:50), until the flame stabilizes below the sample (7:30). There, pyrolysis gases are transported downwards via the open vertical wood vessels, supplying the second flame with flammable gas. Experiments performed with horizontal grain orientations (not reported here) have no such flame stabilization below the sample. Instead, flames anchor around the two vertical faces oriented along the vessels, confirming the current interpretation.

4.3. Measurements of pyrolysis and oxidation

Volume-averaged measurements of pyrolysis and oxidation speeds are computed from the density field of the sample at each XCT scan. For this, the mass of the biomass and that of the char are evaluated by integrating the density field over the respective volumes. The corresponding mass rates of biomass and char, $\dot{m}_b$ and $\dot{m}_c$, are then obtained by differentiation in time. It is then assumed that the pyrolysis of 1 kg of biomass results in $(1-\alpha)$ kg of char and α kg of gases, where α is the mass fraction of volatile content in the biomass, assumed to be homogeneous over the sample. Mass rates of the pyrolysis $\dot{m}_p$ and oxidation $\dot{m}_o$ are then obtained as

$$\dot{m}_p = -\alpha \dot{m}_b \,, \tag{3a}$$

$$\dot{m}_o = -(1-\alpha)\dot{m}_b - \dot{m}_c \,. \tag{3b}$$

To determine α from Eq. (3b), $\dot{m}_b$ and $\dot{m}_c$ are measured at pyrolysis conditions, for which $\dot{m}_o = 0$. This is achieved by placing samples further downstream of the burner, at a height above the burner of $h = 10$ cm, thereby reducing the heat flux to the samples. For these reduced heating conditions, neither smoldering nor flaming is visually

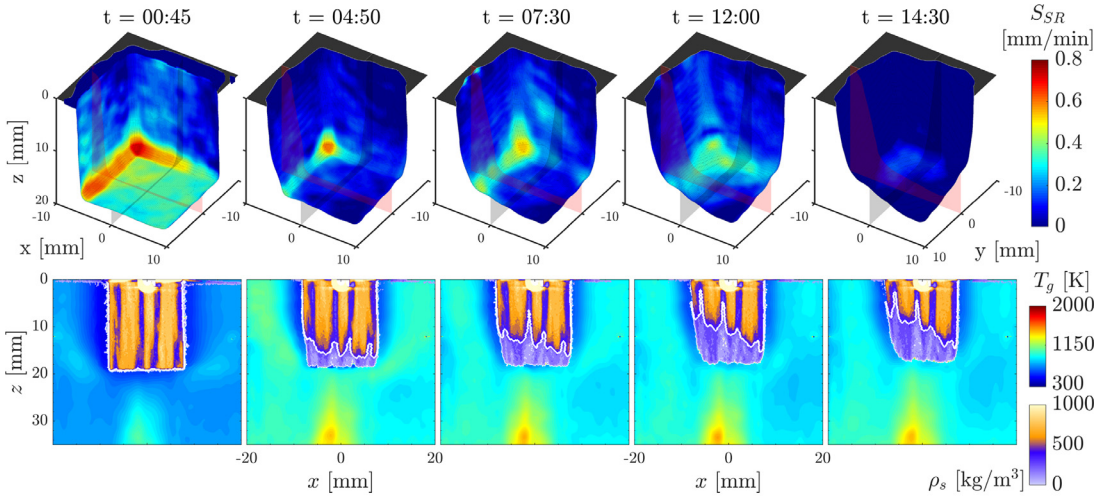

(a) 6% O_2, with partial pyrolysis.

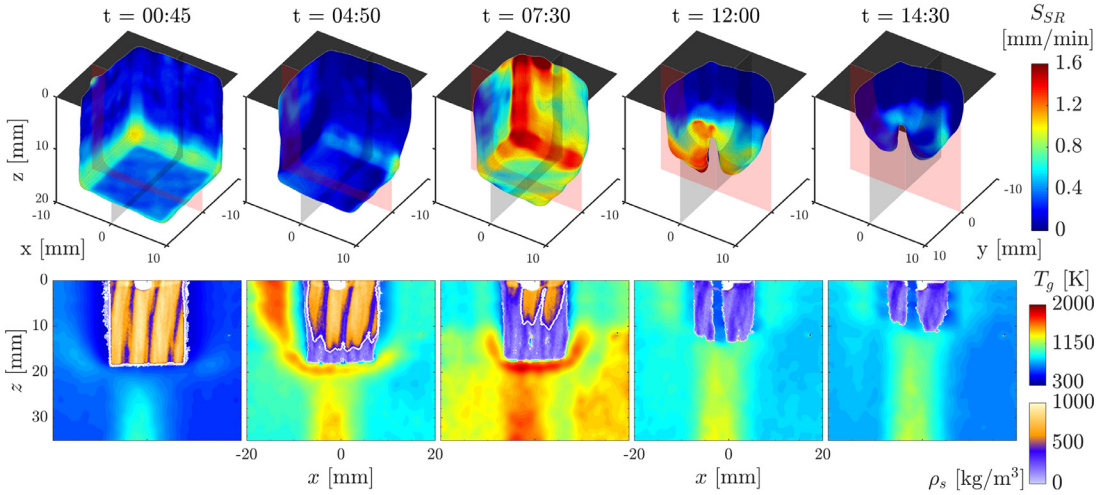

(b) 11% O_2, with complete pyrolysis.

Fig. 4. X-ray measurements showing 3D solid contours with color coding of local surface recess speed S_{SR} and vertical cross-sections at $y = 0$ of simultaneous gas temperature and solid density for (a) 6% O_2 and (b) 11% O_2. The $y = 0$ plane is shown in red in the 3D figures.

observed, and pure pyrolysis conditions are established. The volatile mass fraction is evaluated at these conditions as $\alpha = 0.81 \pm 0.03$, a value which is used to infer rates of pyrolysis and oxidation over time. This result is in reasonable agreement with the volatile content of 83.4 % measured by proximate analysis. Propagation speeds of the pyrolysis and oxidation fronts are then obtained from Eqs. (2a) and (2b), by using measurements of pyrolysis and oxidation areas from XCT surface segmentation. An inorganic content of 0.88% is measured by proximate analysis, and the contribution of ash is consequently neglected in this analysis.

Figure 5 shows the propagation speeds of the oxidation S_o, pyrolysis S_p, and mean surface recess S_{SR} as a function of time for 6% and 11% O_2. The mean surface recess speed S_{SR} is obtained as the surface average of the local surface recess speed reported in Fig. 4. Results show the capabilities of using XCT to measure simultaneous pyrolysis and oxidation rates and capture strong variations between flaming and smoldering regimes.

For 6% O_2, the pyrolysis speeds obtained during flaming are up to 2.5 times larger than those obtained during smoldering. The speeds are up to 3 times higher for 11% O_2 with a maximum of

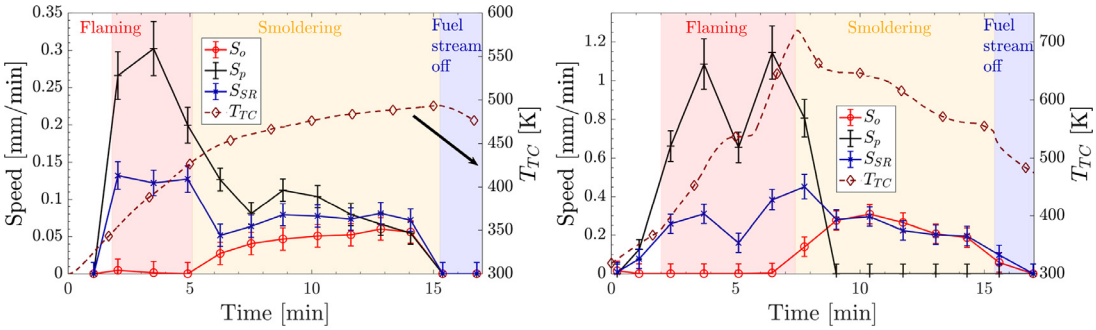

(a) 6% O_2, with partial pyrolysis. (b) 11% O_2, with complete pyrolysis.

Fig. 5. Propagation speeds for oxidation S_o, pyrolysis S_p, and surface recess S_{SR}, and thermocouple temperature T_{TC} over the duration of two experiments with different O_2 concentrations. Vertical error bars are derived from the sensitivity to the segmentation step.

1.15 mm/min for pyrolysis. In both cases, no significant char oxidation is observed during flaming, as the gas phase reaction deprives the sample surface of O_2. Pyrolysis speeds are up to three times larger than surface recess speeds, in agreement with the drop in density by a factor of three from biomass to char. For 11% O_2, a lower speed is seen at 4:50, which corresponds to the time at which the flame moved from the sample side and anchored below the sample. This is associated with a drop in the heat flux, confirmed by the thermocouple measurements. For 11% O_2, the surface recess is only driven by char oxidation after flaming. This is well captured by the near equality measured in the two corresponding speed values. For 6% O_2, the surface recess speed is higher than the char oxidation speed after flaming, as the sample is still shrinking from the on-going pyrolysis.

5. Conclusions

This work reports in-situ 3D X-ray computed tomography measurements of smoldering. Solid density and gas phase temperature were simultaneously measured during the smoldering of oak biomass samples operated at different oxidation conditions. Sub-millimeter spatial resolution and temporal resolution of 90 s were achieved, enabling to capture the unsteady 3D dynamics of smoldering. These experiments revealed effects of biomass grain structures on flaming stabilization and pyrolysis fingering, and the role of crack formation in char oxidation. Mass evaluations via XCT were quantitatively compared with load cell measurements, showing good agreement. A volumetric model was developed to determine the propagation speeds of pyrolysis and char oxidation from XCT measurements, and comparisons with surface recess speed were performed to further analyze the coupled kinematics inherent to smoldering.

Due to the low rates of pyrolysis and oxidation, X-ray diagnostics offer opportunities for investigating smoldering. The penetrating nature of X-rays enables the application to a broad range of solid fuels from porous foam to denser materials such as wood or peat. The reduced photon counts and the slow acquisition rates remain key limitations towards extending XCT to biomass combustion. However, recent progress on the development of high intensity synchrotron sources [21] and fast X-ray acquisition systems [26] offer opportunities for extending the range of operating conditions.

Declaration of Competing Interest

The authors declare that they have no known competing financial interests or personal relationships that could have appeared to influence the work reported in this paper.

Acknowledgments

This work was supported by the NSF (Award No. CBET-1800906), FM Global, and DFG Mercator Fellowship (SPP1980 “SpraySyn: Nanopartikelsynthese in Sprayflammen”). Discussions with Prof. C. T. Bowman and Prof. R. Mitchell are acknowledged. We would like to thank Vincent Xia for his help in conducting the experiments.

References

[1] G. Rein, SFPE Handbook of Fire Protection Engineering, fifth ed., Springer, 2016, pp. 581–603.
[2] B. Poulter, N.L. Christensen, P.N. Halpin, *J. Geophys. Res. Atmos.* 111 (D6) (2006) 301.
[3] E.R. Rabelo, C.A. Veras, J.A. Carvalho, E.C. Alvarado, D.V. Sandberg, J.C. Santos, *Atmos. Environ.* 38 (2) (2004) 203–211.

[4] E. Beagle, Y. Wang, D. Bell, E. Belmont, *Bioresour. Technol.* 251 (2018) 31–39.
[5] T.J. Ohlemiller, *Prog. Energy Combust. Sci.* 11 (4) (1985) 277–310.
[6] R.S. Miller, J. Bellan, *Combust. Sci. Technol.* 126 (1997) 97–137.
[7] X. Huang, G. Rein, *Proc. Combust. Inst.* 37 (2019) 4025–4033.
[8] S. McAllister, M. Finney, *Proc. Combust. Inst.* 36 (2017) 3073–3080.
[9] K. Kuwana, K. Suzuki, Y. Tada, G. Kushida, *Proc. Combust. Inst.* 36 (2017) 3203–3210.
[10] N. Prat-Guitart, G. Rein, R.M. Hadden, C.M. Belcher, J.M. Yearsley, *Int. J. Wildland Fire* 25 (4) (2016) 456–465.
[11] S.D. Tse, R.A. Anthenien, A.C. Fernandez-Pello, K. Miyasaka, *Combust. Flame* 116 (1–2) (1999) 120–135.
[12] O. Putzeys, A. Bar-Ilan, G. Rein, A.C. Fernandez-Pello, D.L. Urban, *Proc. Combust. Inst.* 31 (2007) 2669–2676.
[13] J. Yang, N. Liu, H. Chen, W. Gao, *Proc. Combust. Inst.* 37 (2019) 4073–4081.
[14] S.N. Scott, R.M. Keedy, V.E. Brunini, M.W. Kury, A.B. Dodd, J.L. Urban, A.C. Fernandez-Pello, *Proc. Combust. Inst.* 37 (2019) 4009–4016.
[15] E. Boigné, P. Muhunthan, D. Mohaddes, Q. Wang, S. Sobhani, W. Hinshaw, M. Ihme, *Combust. Flame* 200 (2019) 142–154.
[16] G.H. Fong, S. Jorgensen, S.L. Singer, *Fuel* 224 (2018) 752–763.
[17] N. Hansen, R.S. Tranter, K. Moshammer, J.B. Randazzo, J.P. Lockhart, P.G. Fugazzi, T. Tao, A.L. Kastengren, *Combust. Flame* 181 (2017) 214–224.
[18] J.P. Mathews, Q.P. Campbell, H. Xu, P. Halleck, *Fuel* 209 (2017) 10–24.
[19] K. Jones, G. Ramakrishnan, M. Uchimiya, A. Orlov, *Energy Fuels* 29 (3) (2015) 1628–1634.
[20] T.Y. Chu, W. Gill, J.W. Moore, M.L. Hobbs, L.A. Gritzo, J.L. Moya, *Int. SAMPE Symp. Exhib.* 41 (1) (1996) 722–734.
[21] A. Kastengren, C.F. Powell, *Exp. Fluids* 55 (2014) 1686.
[22] J. Dunnmon, S. Sobhani, M. Wu, R. Fahrig, M. Ihme, *Proc. Combust. Inst.* 36 (2017) 4399–4408.
[23] J. Als-Nielsen, D. McMorrow, *Elements of Modern X-ray Physics*, John Wiley & Sons, 2011.
[24] R.S. Tranter, A.L. Kastengren, J.P. Porterfield, J.B. Randazzo, J.P.A. Lockhart, J.H. Baraban, G.B. Ellison, *Proc. Combust. Inst.* 36 (3) (2017) 4603–4610.
[25] L.A. Feldkamp, L. Davis, J.W. Kress, *J. Opt. Soc. Am. A* 1 (6) (1984) 612–619.
[26] S.A. Mäkiharju, C. Gabillet, B.G. Paik, N.A. Chang, M. Perlin, S.L. Ceccio, *Exp. Fluids* 54 (7) (2013) 1561.